

Mechanical properties and microdomain separation of polymer-grafted fluid membranes

Hao Wu,* Hayato Shiba, and Hiroshi Noguchi†

Institute for Solid State Physics, University of Tokyo, Kashiwa 277-8581, Chiba, Japan

Abstract

The entropic effects of grafted polymers on biomembranes are studied using simulations of a meshless membrane model combined with anchored linear polymer chains. The bending rigidity and spontaneous curvature are investigated for grafted ideal and excluded-volume polymer chains. Our results agree with the previous theoretical predictions well. It is found that the polymer reduces the line tension of membrane edges, as well as the interfacial line tension between membrane domains, leading to microdomain formation. Instead of the mixing of two phases as seen in typical binary fluids, densely grafted polymers stabilize small domains. A mean field theory is proposed for the edge line tension reduced by grafting ideal chains, which well reproduces our simulation results.

PACS numbers: 87.16.D-, 87.17.Aa, 82.70.Uv

*Email address: wade@issp.u-tokyo.ac.jp, wadewizard@gmail.com

†Email address: noguchi@issp.u-tokyo.ac.jp

I. INTRODUCTION

Our knowledge of the heterogeneous structure of biomembranes has advanced from the primitive fluid mosaic model [1] to the modern raft model [2, 3] over the past decades. According to this modern model membrane proteins are not randomly distributed in lipid membranes but concentrated in local microdomains, called lipid rafts, with a diameter of $10 \sim 100$ nm [4–7]. The raft contains high concentrations of glycosphingolipids and cholesterol, and plays important roles in many intra- and intercellular processes including signal transaction and membrane protein trafficking.

In the last decade, phase separation in multi-component lipid membranes has been intensively investigated in three-component systems of saturated and unsaturated phospholipids and cholesterol [8–15]. Lipid domains exhibit various interesting patterns on the micrometer scale, which can be reproduced by theoretical calculations and simulations. Various shapes of lipid domains can be also formed in the air–water interface [16–18]. However, the formation mechanism of microdomains on the $10 \sim 100$ nm scale has not been understood so far. In lipid rafts, glycolipids contain glycan chains. Recently, network-shaped domains and small scattered domains have been observed in lipid membranes with PEG-conjugated cholesterol [19]. The effects of grafted polymers have been well investigated in the case of uniform grafting on membranes, but the effects on the lipid domains and line tension have not been well investigated. In this paper, we focus on the effects of grafted polymers on the properties of biomembranes, in particular, on lipid domains.

It is well known that grafted polymers modify membrane properties [20]. The polymer grafting induces a positive spontaneous curvature C_0 of the membranes and increases the bending rigidity κ . These relations are analytically derived using the Green’s function method and scaling method [20–24] and confirmed by Monte Carlo simulations [25–27]. Experimentally, the κ increase is measured by micropipette aspiration of liposomes [28]. Polymer decoration can enhance the stability of lipid membranes. PEG-conjugated lipids can reduce protein adsorption and adhesion on cellular surfaces, whereby PEG-coated liposomes can be used as a drug carrier in drug-delivery systems [29, 30].

When vesicles are formed from the self-assembly of surfactant molecules via micelle growth, the vesicle size is determined kinetically by the competition between the bending energy and the line tension energy of the membrane edge [31–37]. Recently, Bressel

et al. reported that the addition of an amphiphilic copolymer induces the formation of larger vesicles [38]. A polymer-grafting-induced liposome-to-micelle transition is also observed [20, 39, 40]. The line tension of the membrane edge is considered to be reduced by polymer grafting, but it has not been systematically investigated so far. In this study, we simulate the line tension of the membrane edge for grafted ideal and excluded-volume chains and analytically investigate the polymer effects on the line tension for ideal chains.

In order to simulate the polymer-grafting effects on biomembranes, we employ one of the solvent-free meshless membrane models [41, 42]. Since we focus on the entropic effects of polymer chains, the detailed structures of the bilayer can be neglected, and thus the membranes can be treated as a curved surface. In the meshless model, a membrane particle represents a patch of bilayer membrane and membrane properties can be easily controlled.

In Sec. II, the membrane model and simulation method are described. In Sec. III, the bending rigidity and spontaneous curvature are estimated from the axial force measurement of cylindrical membranes and are also compared with the previous theoretical predictions. The reduction in the line tension of the membrane edge is discussed for both ideal chains and excluded-volume chains in Sec IV. In Sec V, we present our investigation on the phase separation in two-component membranes with grafted polymer chains. Finally, a summary and discussions are provided in Sec VI.

II. MODEL AND METHOD

In this study, we employ a coarse-grained meshless membrane model with grafted linear polymer chains [42, 43]. One membrane particle possesses only a translational degree of freedom. The membrane particles form a quasi-two-dimensional (2D) membrane according to a curvature potential based on the moving least-squares (MLS) method [42]. Polymer particles are linked by a harmonic potential, and freely move as a self-avoiding chain with a soft-core repulsion. One end of each polymer chain is anchored on a single membrane particle with a harmonic potential and a soft-core repulsion [43].

We consider a single- or multi-component membrane composed of N_{mb} membrane particles. Among them, N_{chain} membrane particles are anchored by polymer chains. Each polymer chain consists of N_p polymer segments with an anchored membrane particle. The

membrane and polymer particles interact with each other via a potential

$$U_{\text{tot}} = U_{\text{rep}} + U_{\text{mb}} + U_{\text{p}} + U_{\text{AB}}, \quad (1)$$

where U_{rep} is an excluded-volume potential, U_{mb} is a membrane potential, U_{p} is a polymer potential, and U_{AB} is a repulsive potential between different species of membrane particles in two-component membranes.

All particles have a soft-core excluded-volume potential with a diameter of σ .

$$U_{\text{rep}} = \varepsilon \sum_{i < j} \exp [-20(r_{ij}/\sigma - 1) + B] f_{\text{cut}}(r_{ij}/\sigma) \quad (2)$$

in which r_{ij} is the distance between membrane (or polymer) particles i and j . The diameter σ is used as the length unit, $B = 0.126$, and $f_{\text{cut}}(s)$ is a C^∞ cutoff function

$$f_{\text{cut}}(s) = \begin{cases} \exp \left\{ A \left[1 + \frac{1}{(|s|/s_{\text{cut}})^n - 1} \right] \right\} & (s < s_{\text{cut}}) \\ 0 & (s \geq s_{\text{cut}}) \end{cases} \quad (3)$$

with $n = 12$, $A = 1$, and $s_{\text{cut}} = 1.2$.

For excluded-volume polymer chains, all pairs of particles including pairs of polymer segments have the repulsive interaction given in Eq. 2. In contrast, for ideal polymer chains, polymer segments have the excluded-volume interactions only with membrane particles to prevent polymer segments from passing through the membrane.

A. Meshless membrane model

The membrane potential U_{mb} consists of attractive and curvature potentials,

$$U_{\text{mb}} = \sum_i^{N_{\text{mb}}} [\varepsilon U_{\text{att}}(\rho_i) + k_\alpha \alpha_{\text{pl}}(\mathbf{r}_i)], \quad (4)$$

where the summation is taken only over the membrane particles. The attractive multibody potential is employed to mimic the “hydrophobic” interaction.

$$U_{\text{att}}(\rho_i) = 0.25 \ln \{1 + \exp [-4(\rho_i - \rho^*)]\} - C, \quad (5)$$

which is a function of the local density of membrane particles

$$\rho_i = \sum_{j \neq i}^{N_{\text{mb}}} f_{\text{cut}}(r_{ij}/\sigma), \quad (6)$$

with $n = 12$, $s_{\text{half}} = 1.8$, and $s_{\text{cut}} = s_{\text{half}} + 0.3$, where $f_{\text{cut}}(s_{\text{half}}) = 0.5$, which implies $A = \ln(2)\{(s_{\text{cut}}/s_{\text{half}})^n - 1\}$. The constant $C = 0.25 \ln[1 + \exp(4\rho^*)]$ is chosen so that $U_{\text{att}} = 0$ at $\rho_i = 0$. Here we set $\rho^* = 6$ in order to simulate a 2D fluid membrane. For $\rho_i < \rho^*$, U_{att} acts as a pairwise potential with $U_{\text{att}} = -2 \sum_{j>i} f_{\text{cut}}(r_{ij}/\sigma)$. For $\rho_i \gtrsim \rho^*$, this potential saturates to the constant $-C$. Thus, it is a pairwise potential with a cutoff at densities higher than ρ^* .

The curvature potential is expressed by the shape parameter called “aplanarity”, which is defined by

$$\alpha_{\text{pl}} = \frac{9D_w}{T_w M_w}, \quad (7)$$

with the determinant $D_w = \lambda_1 \lambda_2 \lambda_3$, the trace $T_w = \lambda_1 + \lambda_2 + \lambda_3$, and the sum of the principal minors $M_w = \lambda_1 \lambda_2 + \lambda_2 \lambda_3 + \lambda_3 \lambda_1$. The aplanarity α_{pl} scales the degree of deviation from the planar shape, and λ_1 , λ_2 , and λ_3 are three eigenvalues of the weighted gyration tensor

$$a_{\alpha\beta}(\mathbf{r}_i) = \sum_j^{N_{\text{mb}}} (\alpha_j - \alpha_G)(\beta_j - \beta_G) w_{\text{cv}}(r_{ij}), \quad (8)$$

where $\alpha, \beta \in \{x, y, z\}$, and the mass center of a local region of the membrane $\mathbf{r}_G = \sum_j \mathbf{r}_j w_{\text{cv}}(r_{ij}) / \sum_j w_{\text{cv}}(r_{ij})$. Without loss of generality, we suppose that $\lambda_1 \leq \lambda_2 \leq \lambda_3$. The minimum eigenvalue λ_1 represents a deviation from the local plane fit by the neighboring membrane particles, and its corresponding eigenvector is collinear with the normal vector \mathbf{n} of this plane. When the i -th membrane particle has two or fewer neighbor particles within the cutoff distance r_{cc} , they could be localized on a certain plane, and therefore, $\alpha_{\text{pl}} = 0$. A truncated Gaussian function is employed to calculate the weight of the gyration tensor

$$w_{\text{cv}}(r_{ij}) = \begin{cases} \exp\left[\frac{(r_{ij}/r_{\text{ga}})^2}{(r_{ij}/r_{\text{cc}})^n - 1}\right] & (r_{ij} < r_{\text{cc}}) \\ 0 & (r_{ij} \geq r_{\text{cc}}), \end{cases} \quad (9)$$

which is smoothly cut off at $r_{ij} = r_{\text{cc}}$. Here we use the parameters $n = 12$, $r_{\text{ga}} = 0.5r_{\text{cc}}$, and $r_{\text{cc}} = 3\sigma$. The bending rigidity and the line tension of the membrane edges are linearly dependent on k_α and ε , respectively, for $k_\alpha \gtrsim 10$, so that they can be independently varied by changing k_α and ε , respectively.

B. Anchored Polymer Chain

We consider flexible linear polymer chains anchored on the membrane. Polymer particles are connected by a harmonic spring potential,

$$U_p = \frac{k_{\text{bond}}}{2} \sum_{\text{chains}} (r_{i,i+1} - b)^2, \quad (10)$$

where k_{bond} is the spring constant for the harmonic potential and b is the Kuhn length of the polymer chain. The summation is taken only between neighboring particles along polymer chains and between the end polymer particles and anchored membrane particles (a total of N_p springs in each chain). We choose $b = 1.2\sigma$ here so that a polymer chain can stay in the force-free state for $r_{i,i+1} = b$.

C. Two-component membrane

Two types of membrane particles, A and B, are considered in Sec. V. The number of these particles are N_A and N_B , respectively. To investigate phase separation, we apply a repulsive term U_{AB} in Eq. 1 to reduce the chemical affinity between different types of membrane particles [44]. The potential U_{AB} is a monotonic decreasing function: $U_{AB} = \varepsilon_{AB} \sum_{i \in A, j \in B} A_1 f_{\text{cut}}(r_{i,j})$ with $n = 1$, $A_1 = 1$ and $r_{\text{cut}} = 2.1\sigma$, and $A_1 = \exp[\sigma/(r_{\text{cut}} - \sigma)]$ to set $U_{AB}(\sigma) = 1$.

D. Simulation method

The NVT ensemble (constant number of particles N , volume V , and temperature T) is used with periodic boundary conditions in a simulation box of dimensions $L_x \times L_y \times L_z$. For planar membranes, the projected area $L_x \times L_y$ is set for the tensionless state. The dynamics of both membrane and anchored flexible polymers are calculated by using underdamped Langevin dynamics. The motions of membrane and polymer particles are governed by

$$m \frac{d^2 \mathbf{r}_i}{dt^2} = -\frac{\partial U_{\text{tot}}}{\partial \mathbf{r}_i} - \zeta \frac{d\mathbf{r}_i}{dt} + \mathbf{g}_i(t) \quad (11)$$

where m is the mass of a particle (membrane or polymer particle) and ζ is the friction constant. $\mathbf{g}_i(t)$ is a Gaussian white noise, which obeys the fluctuation-dissipation theorem:

$$\langle g_{i,\alpha}(t) \rangle = 0, \quad (12)$$

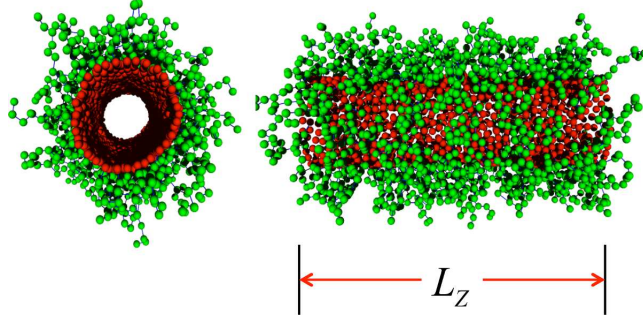


FIG. 1: Front and side views of a snapshot of a cylindrical membrane with grafted excluded-volume polymer chains at the polymer density $\phi = 0.167$ and cylinder axial length $L_z = 45.3\sigma$. The red and green particles represent membrane and polymer particles, respectively.

$$\langle g_{i,\alpha}(t)g_{j,\beta}(t') \rangle = 2k_B T \zeta \delta_{ij} \delta_{\alpha\beta} \delta(t - t'),$$

where $\alpha, \beta \in \{x, y, z\}$, $k_B T$ is the thermal energy, and $\langle \dots \rangle$ denotes the statistical average. We employ the time unit $\tau = \zeta \sigma^2 / k_B T$ with $m = \zeta \tau$. The Langevin equations are integrated by the leapfrog algorithm [45] with a time step of $\Delta t = 0.005\tau$.

We use $N_p = 10$, $\varepsilon = 4$, $k_\alpha = 10$, and $k_{\text{bond}} = 10$ throughout this study. In the absence of grafted polymer chains, the tensionless membranes have a bending rigidity of $\kappa/k_B T = 21 \pm 0.5$, the line tension of the open edges $\Gamma_{\text{ed}}\sigma/k_B T = 4.5$ and the area $a_0 = 1.44\sigma^2$ per membrane particle [46]. For single-component membranes, the number of membrane particles is fixed as $N_{\text{mb}} = 1200$ and the number fraction $\phi = N_{\text{chain}}/N_{\text{mb}}$ of polymer-anchored membrane particles is varied. For two-component membranes the number of the type A membrane particles is fixed as $N_A = 400$, and the number of the type B particles is chosen as $N_B = 400$ and 2100 for a striped domain and a circular domain, respectively. The polymer chains are anchored to the type A particles and the polymer fraction $\phi = N_{\text{chain}}/N_A$ is varied. To confirm that the membranes are in thermal equilibrium, we compare the results between two initial states, stretching or shrinking, and check that no hysteresis has occurred. We slowly stretch and shrink cylindrical or striped membranes in the axial direction with a speed less than $dL_z/dt = 10^{-6}\sigma/\tau$ and then equilibrate them for $t/\tau = 6 \times 10^4$ before the measurements. For the simulations of circular domains, the membranes were equilibrated for a duration of $6 \times 10^4\tau$ after step-wise changes of ε_{AB} . The error bars are calculated from six independent runs.

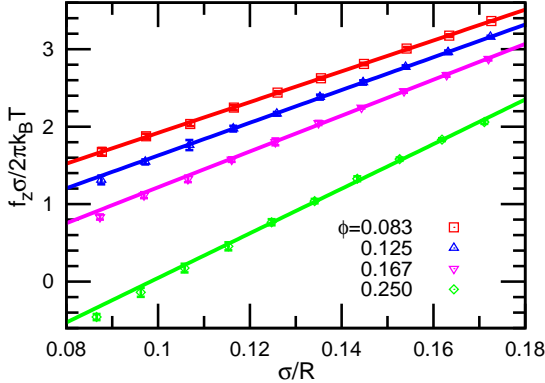


FIG. 2: Force f_z dependence on the radius R of the cylindrical membranes with anchored excluded-volume chains at $\phi = 0.083, 0.125, 0.167$, and 0.250 . The solid lines are obtained by linear least-squares fits.

III. BENDING RIGIDITY AND SPONTANEOUS CURVATURE OF MEMBRANES

A cylindrical membrane with polymer chains anchored outside the membrane is used to estimate the polymer-induced spontaneous curvature and bending rigidity (see Fig. 1). For a cylindrical membrane with radius R and length L_z , the Helfrich curvature elastic free energy is given by

$$\begin{aligned} F_{cv} &= \int \left[\frac{\kappa}{2} (C_1 + C_2 - C_0)^2 + \bar{\kappa} C_1 C_2 \right] dA \\ &= 2\pi R L_z \left[\frac{\kappa}{2} \left(\frac{1}{R} - C_0 \right)^2 \right], \end{aligned} \quad (13)$$

where C_1 and C_2 are the principal curvatures at each position on the membrane surface, and the membrane area $A = 2\pi R L_z$. The coefficients κ and $\bar{\kappa}$ are the bending rigidity and the saddle-splay modulus, respectively, and C_0 is the spontaneous curvature. In the absence of the grafted polymers (we call it a pure membrane hereinafter), the membrane has zero spontaneous curvature, $C_0 = 0$.

The membrane also has an area compression energy $F_{ar}(A)$: $F_{ar}(A) = K_A (A - A_0)^2 / 2A_0$ for $A - A_0 \ll A_0$, where A_0 is the area of the tensionless membrane. The radius R is determined by free-energy minimization $\partial F / \partial R|_{L_z} = 0$ for $F = F_{cv} + F_{ar}(A)$. Since the curvature energy increases with increasing L_z , a shrinking force

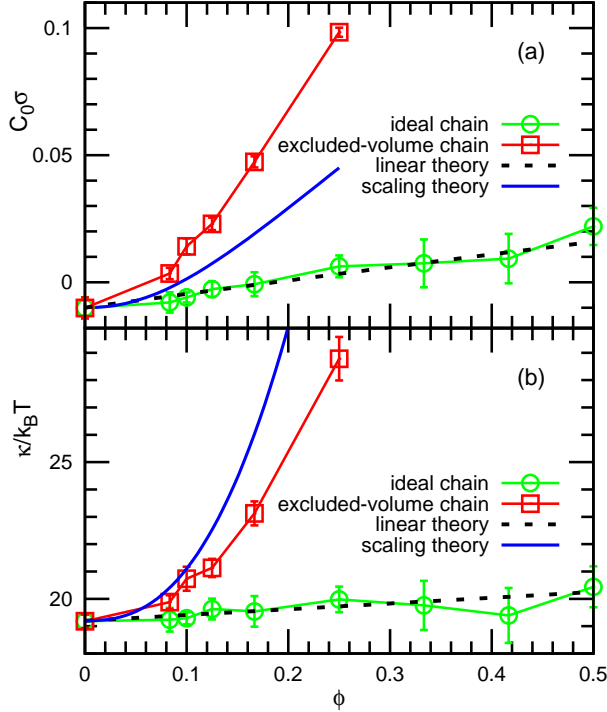


FIG. 3: Polymer density ϕ dependence of (a) the spontaneous curvature C_0 and (b) bending rigidity κ of the membranes with anchored ideal chains and excluded-volume chains. The dashed lines in (a) and (b) represent the prediction of the linear theory (Eqs. 16 and 17) for the ideal chains. The solid lines in (a) and (b) represent the prediction of the scaling theory (Eqs. 18 and 19) in the brush region.

$$f_z = \frac{\partial F}{\partial L_z} \Big|_R = 2\pi\kappa \left(\frac{1}{R} - C_0 \right). \quad (14)$$

is generated along the cylindrical axis.

Figure 2 shows the axial force f_z calculated from the pressure tensors,

$$P_{\alpha\alpha} = (Nk_B T - \sum_i \alpha_i \frac{\partial U}{\partial \alpha_i})/V, \quad (15)$$

for $\alpha \in \{x, y, z\}$, where the summation is taken over all membrane and polymer particles. When the potential interaction crosses the periodic boundary, the periodic image $\alpha_i + nL_\alpha$ is employed for $P_{\alpha\alpha}$ calculation. The force f_z increases linearly with $1/R$ [43]. Thus, C_0 and κ of the grafted membranes can be estimated from a linear fitting method to Eq. 14. For both anchored ideal chains and excluded-volume chains, the obtained values of C_0 and κ are shown in Fig. 3. For the pure membranes, the value of κ agrees very well with those estimated

from the height fluctuations of planar membranes [46] and membrane buckling [47]. The estimated value of C_0 for the pure membrane deviates slightly from the exact value, zero. This small deviation would be caused by a higher-order term of the curvature energy [48] or finite size effects as discussed in Ref. [46].

The anchored polymer generates a positive spontaneous curvature, and enhances the bending rigidity κ . Both quantities increase with increasing polymer chain density, and for the excluded-volume chains, these increases are enhanced by the repulsive interactions between the neighboring chains.

In the mushroom region, the spontaneous curvature and bending rigidity are linearly dependent on the polymer density ϕ . Analytically, the relations [22, 23]

$$\kappa\Delta C_0 = 2a_{\text{sp}}k_{\text{B}}TR_{\text{end}}\phi/a_0 \quad (16)$$

$$\Delta\kappa = a_{\kappa}k_{\text{B}}TR_{\text{end}}^2\phi/a_0 \quad (17)$$

are predicted, where ΔC_0 and $\Delta\kappa$ are the differences of the spontaneous curvatures and bending rigidities between the polymer-decorated membrane and the pure membrane, respectively, and R_{end} is the mean end-to-end distance of the polymer chain. The factor 2 in Eq. 16 appears because in our definition the spontaneous curvature is twice as large as that in the previous works [22, 23, 25]. The coefficients are derived analytically using the Green's function [22, 23] and also estimated by Monte Carlo simulations of single anchored polymer chains [25]: $a_{\kappa} = 0.21$ and 0.2 ; and $a_{\text{sp}} = 0.18$ and 0.17 for ideal and excluded-volume chains, respectively. Our results for the ideal chains agree very well with these previous predictions (compare the dashed lines and symbols in Fig. 3). To draw the dashed line in Fig. 3(a), the end-to-end distance is estimated from the simulation; $R_{\text{end}} = 4.16\sigma$, which is slightly larger than a free polymer chain $R_{\text{end}} = \sqrt{N_{\text{p}}}b = 3.79\sigma$. Note that grafted ideal polymer chains can be considered in the mushroom region for any density ϕ , since the polymer chains do not directly interact with each other.

For excluded-volume chains, our results deviate from the theoretical predictions (Eq. 16) for the mushroom region at $\phi \gtrsim 0.1$. Thus, in the high density of anchored polymer chains, the interactions between polymer chains are not negligible. We compare our results with a scaling theory based on a blob picture for the brush region in Ref [23]. We extract the numerical results from the nonlinear equation for a cylindrical surface [23]

$$\frac{\partial f_c(x)}{\partial x} + \frac{4\kappa_0}{k_{\text{B}}T}N_{\text{p}}^{-3}\bar{\Gamma}^{-3/2\nu}x = 0. \quad (18)$$

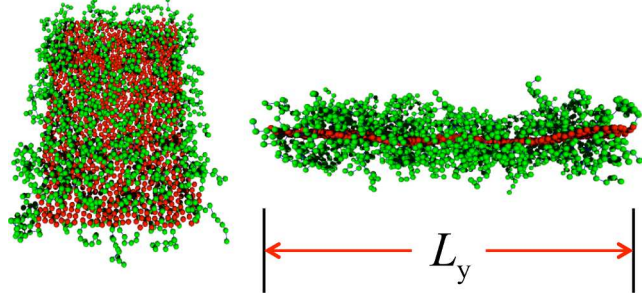


FIG. 4: Top and side views of a snapshot of a membrane strip with grafted excluded-volume chains at $\phi = 0.15$ and the length $L_y = 57.6\sigma$ of each membrane edge.

where $f_c(x) = [\{1 + (1 + \nu)x/\nu\}^{\nu/(1+\nu)} - 1]/x - 1$, the bending rigidity κ_0 of the pure membrane, and the reduced spontaneous curvature $x = h_0C_0/2$ for the height of a brush on a flat surface $h_0 = N_p\bar{\Gamma}^{(1-\nu)/2\nu}b$. The polymer coverage on the membrane is normalized by the maximum coverage as $\bar{\Gamma} = \Gamma/\Gamma_{\max} = b^2\phi/a_0$, and the exponent $\nu = 0.6$ is used for excluded-volume chains. The bending rigidity is given by

$$\Delta\kappa = \frac{\nu + 2}{12\nu^2} N_p^3 \bar{\Gamma}^{3/2\nu} k_B T \quad (19)$$

in the small curvature limit [23]. Our results qualitatively agree with these predictions from the scaling theory (see Fig. 3). The deviation is likely due to the polymer length ($N_p = 10$) in the simulation, which is too short to apply the blob picture in the scaling theory.

IV. LINE TENSION OF MEMBRANE EDGES

A. Simulation results

Next, we investigate the line tension of membrane edges with various anchored polymer densities for both ideal chains and excluded-volume chains. A strip of single-component membrane with grafted polymers is used to estimate the line tension Γ_{ed} of the membrane edges (see Fig. 4). The line tension Γ_{ed} on the edge can be calculated by [46, 49, 50]

$$\Gamma_{\text{ed}} = \frac{\partial F}{2\partial L_y} = \left\langle \frac{P_{xx} + P_{zz}}{2} - P_{yy} \right\rangle \frac{L_x L_z}{2}, \quad (20)$$

since the total edge length is $2L_y$. The pressure $P_{xx} = P_{zz} \approx 0$ for solvent-free simulation with a negligibly low critical micelle concentration. We checked that the line tension is

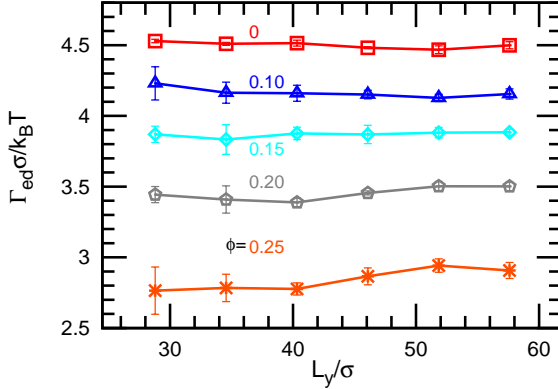


FIG. 5: Line tension Γ_{ed} on the open edge of a membrane strip with grafted excluded-volume chains estimated for different edge lengths L_y at $\phi = 0, 0.1, 0.15, 0.2$, and 0.25 .

independent of the length of the membrane edge for pure membranes as well as for polymer-decorated membranes (see Fig. 5).

Figure 6 shows that the line tension Γ_{ed} decreases with increasing polymer density ϕ . The reduction for excluded-volume chains is much larger than that for ideal chains, similar to polymer effects on the bending rigidity. The polymer chains prefer staying on the edge, since there is more space to move so that they can gain entropy. Figure 7(a) shows that the polymer density distribution ρ_{chain} is nonuniform at the distance d_w from the strip's central axis. High peaks of ρ_{chain} are found close to the edges for both ideal chains and excluded-volume chains, while the density ρ_{mb} of all membrane particles has only very small peak. The relative polymer density $\rho_{\text{chain}}/\rho_{\text{mb}}$ more rapidly increases at the edges for larger mean density ϕ [see Fig. 7(b)]. The mean polymer density ϕ_1 at the edges is calculated as an average $\langle \sum_{d_w \geq d_w^{\max}} \rho_{\text{chain}} / \sum_{d_w \geq d_w^{\max}} \rho_{\text{mb}} \rangle$ for the right region of the peak (d_w^{\max}) of ρ_{mb} in Fig. 7(a). The density difference from the mean value $\Delta\phi = \phi_1 - \phi$ increases with increasing ϕ as shown in Fig. 8. The excluded volume chains induce higher polymer concentration at the edges than the ideal chains.

B. Theoretical analysis

Here we propose a mean field theory for the line tension induced by the grafted polymers in the mushroom region. According to the nonuniform polymer distribution on the membrane strip, we divide the membrane into two regions, an edge (region 1) and middle region (region

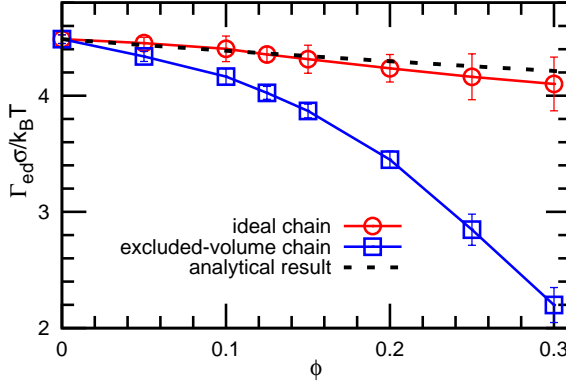


FIG. 6: Polymer density dependence ϕ of the line tension of the membrane edges for ideal and excluded-volume chains. The dashed line represents our theoretical prediction by Eq. 25.

2). The polymer density is assumed to be uniform in each region. The area fractions of the two regions are n_1 and n_2 with $n_1 + n_2 = 1$, and the polymer densities are ϕ_1 and ϕ_2 with $\phi = n_1\phi_1 + n_2\phi_2$. The width of region 1 is considered the radius of gyration of polymer R_g , so that the area fraction is given by

$$n_1 = \frac{2L_y R_g}{N_{mb} a_0}. \quad (21)$$

The free energy of the membrane strip is written as

$$\begin{aligned} \frac{F_{ed}}{N_{mb} k_B T} = & n_1 \phi_1 \ln \phi_1 + n_1 (1 - \phi_1) \ln (1 - \phi_1) \\ & + n_2 \phi_2 \ln \phi_2 + n_2 (1 - \phi_2) \ln (1 - \phi_2) \\ & - n_1 \phi_1 \Delta S + f_0 \end{aligned} \quad (22)$$

where f_0 is the free energy contribution of the membrane without polymer grafting. The first four terms are the mixing entropy for regions 1 and 2. When a polymer chain moves from the middle region to the open edges, it gains the conformational entropy ΔS .

The partition function of a single grafted polymer chain is expressed as $Z_p = q^{N_p} W$, where q is the number of the nearest neighbors in the lattice model ($q = 6$ in a cubic lattice). The restricted weight of a polymer anchored on the flat membrane is $W_{hs} = \text{erf} \left[\frac{\sqrt{q} l_{an}}{2R_{end}} \right]$, where $\text{erf}(x)$ is the error function and l_{an} is the anchor length [22, 23]. On the other hand, the free end of a polymer anchored on the edge can also move the other half space, and has a larger value of weight W_{ed} . We numerically counted the weights W_{ed} and W_{hs} in a cubic lattice.

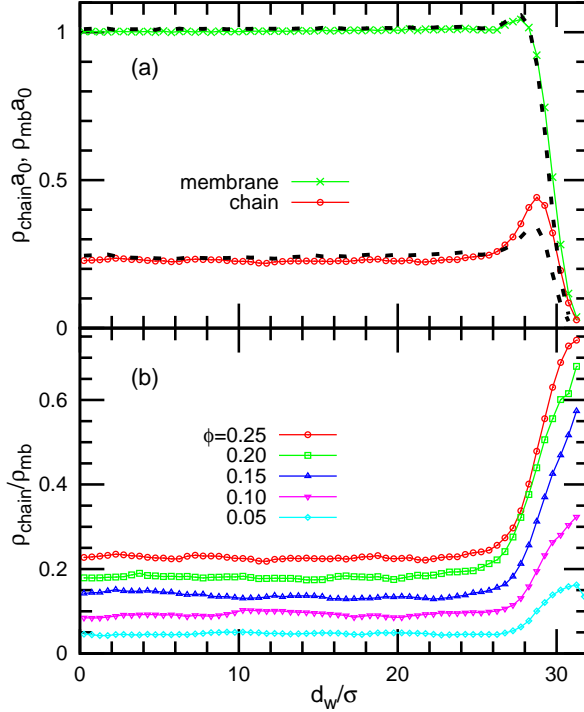


FIG. 7: Density distribution in the membrane strip. (a) Density of polymer-anchored membrane particles ρ_{chain} , and total density ρ_{mb} at $\phi = 0.25$. The solid lines with symbols and dashed lines represent the data for the excluded-volume chains, and ideal chains, respectively. (b) Density ratio $\rho_{\text{chain}}/\rho_{\text{mb}}$ for the excluded-volume chains. The distance d_w from the center of the strip is taken in the direction perpendicular to the edge. The membrane lengths are $L_{\text{st}} = 60\sigma$ perpendicular to the edge and $L_y = 28.8\sigma$ along the edge.

The ratio $W_{\text{ed}}/W_{\text{hs}}$ increases with increasing N_p , and $W_{\text{ed}}/W_{\text{hs}} \simeq 2$ for $N_p = 10$. Thus, the excess entropy is estimated as $\Delta S = \ln(W_{\text{ed}}/W_{\text{hs}}) \simeq \ln 2$ for our simulation condition.

Using minimization of F_{ed} , the polymer density ϕ_1 in the edge region is analytically derived as

$$\begin{aligned} \phi_1 &= \frac{2Q\phi}{s + \sqrt{s^2 - 4Q(Q-1)\phi n_1}} \\ &= \frac{Q\phi}{1 + (Q-1)\phi} \left(1 - \frac{(Q-1)(1-\phi)}{\{1 + (Q-1)\phi\}^2} n_1 \right) + O(n_1^2) \end{aligned} \quad (23)$$

where $Q = \exp(\Delta S)$ and $s = 1 + (Q-1)(\phi + n_1)$. At $Q = 2$ and $n_1 \ll 1$, the density difference is simply $\Delta\phi \equiv \phi_1 - \phi = \phi(1-\phi)/(1+\phi)$, which agrees very well with the simulation results (see Fig. 8).

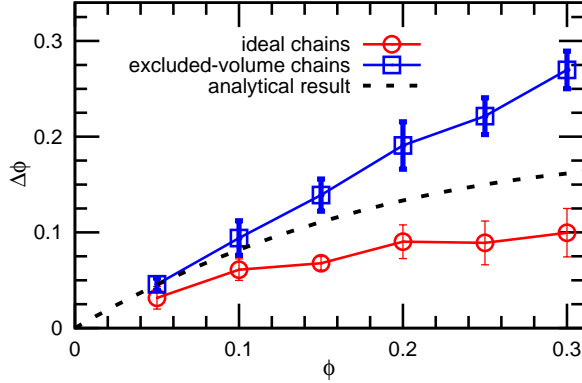


FIG. 8: Excess polymer density $\Delta\phi \equiv \phi_1 - \phi$ at the membrane edge as a function of the mean polymer density ϕ . The solid lines with circles and squares represent our simulation results for the ideal chains and excluded volume chains, respectively. The dashed line represents our theoretical prediction for the ideal chains by Eq. 23.

The line tension is derived as $\Gamma_{\text{ed}} = \partial F_{\text{ed}} / \partial L_{\text{ed}}$, where L_{ed} is the total edge length $L_{\text{ed}} = 2L_y$. Thus, the polymer-induced line tension $\Delta\Gamma_{\text{ed}}$ is given by

$$\frac{\Delta\Gamma_{\text{ed}}a_0}{R_g k_B T} = \ln(1 - n_1) + \phi_1 \ln \frac{\phi_1}{Q(\phi - \phi_1 n_1)} + (1 - \phi_1) \ln \frac{1 - \phi_1}{1 - \phi - (1 - \phi_1)n_1}. \quad (24)$$

At $Q = 2$, the Taylor expansion gives

$$\frac{\Delta\Gamma_{\text{ed}}a_0}{R_g k_B T} = -\ln(1 + \phi) + \frac{\phi(1 - \phi)}{(1 + \phi)^2} n_1 + O(n_1^2). \quad (25)$$

Thus, the line tension Γ_{ed} decreases with increasing ϕ and is independent of the edge length L_y for $n_1 \ll 1$. Figure 6 shows the comparison of line tensions between our simulation and the theoretical results for ideal chains; The agreement is excellent. As the membrane strip becomes narrower (n_1 increases), the polymer effect on the line tension Γ_{ed} is reduced by the loss of mixing entropy in region 2, and Γ_{ed} increases with increasing edge length L_y .

V. TWO-COMPONENT MEMBRANES WITH GRAFTED POLYMER

In this section, we focus on the effects of polymer-grafting-induced interfacial tension. First, in Sec. V A we estimate the line tension of polymer-grafted membrane domains, and then in Sec. V B we investigate the polymer effects on domain separation and domain shape

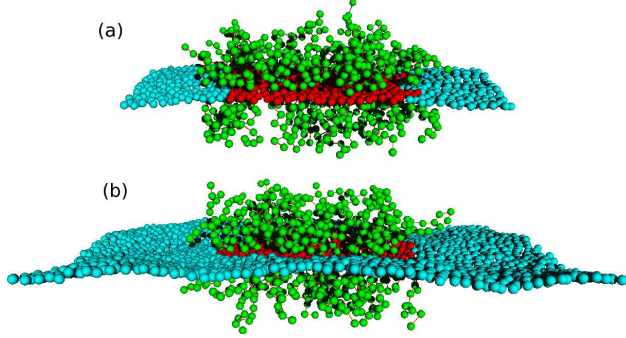


FIG. 9: Snapshots of (a) striped and (b) circular domains with grafted excluded-volume chains in two-component planar membranes at $N_A = 400$ and $\phi = 0.3$. Type A and B membrane particles are displayed in red and blue, respectively.

transformation. Here, we investigate only the membranes with excluded-volume chains, since the effects of the ideal chains are considered to be very small. As described in Sec. III, polymers can induce an effective spontaneous curvature in the membrane. In order to diminish the influence of the induced spontaneous curvature, we symmetrically graft polymer chains on both sides of the membrane as shown in Fig. 9. Half of the chains ($N_{\text{chain}}/2$) are grafted on the upper (lower) side of the membrane, and each chain is anchored on one membrane particle. Then, the net curvature effects induced on both sides of the membrane cancel each other out.

A. Interfacial line tension between two membrane domains

The line tension Γ_{AB} between the type A and B domains is estimated by two methods using a striped domain and a circular domain. For the striped domain shown in Fig. 9(a), the line tension is calculated by

$$\Gamma_{AB} = \langle P_{xx} - P_{yy} \rangle L_x L_z / 2. \quad (26)$$

The obtained line tension for tensionless membranes is shown by solid lines in Fig. 10. We ensured that Γ_{AB} is independent of the boundary length L_y for $24 < L_y/\sigma < 48$ (data not shown). The line tension Γ_{AB} decreases with increasing ϕ , while Γ_{AB} increases with increasing ε_{AB} . Thus, the same value of Γ_{AB} can be obtained for different polymer densities ϕ by adjusting ε_{AB} .

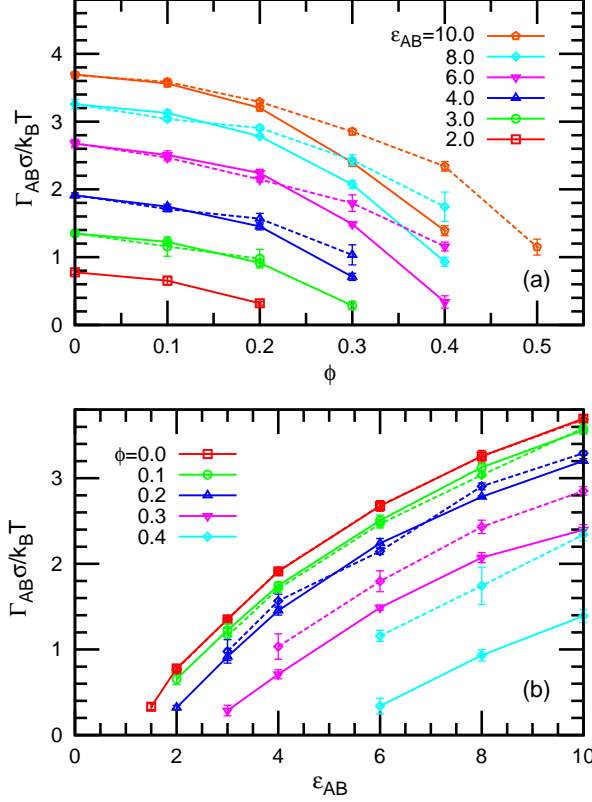


FIG. 10: Interfacial line tension Γ_{AB} between membrane domains as a function of (a) ϕ and (b) ε_{AB} . The solid and dashed lines represent Γ_{AB} estimated from the striped domain and the circular domain, respectively.

Before investigating polymer effects on the domain shapes in the next subsection, we also estimate Γ_{AB} from the circular domain shown in Fig. 9(b). The line tension Γ_{AB} is calculated by the 2D Laplace pressure, [44, 49]

$$\Gamma_{AB} = \bar{R} \Delta \gamma, \quad (27)$$

where \bar{R} is the average radius of the domain, and $\Delta \gamma$ is the difference of surface tension between the type A and B domains: $\Delta \gamma = \gamma^{in} - \gamma^{out}$, where γ^{in} is the surface tension of the inner (type A) domain and γ^{out} is that of the outer (type B) domain. Both of them can be estimated by the pressure tensors of the local regions

$$\gamma^\alpha = \langle P_{zz}^\alpha - (P_{xx}^\alpha + P_{yy}^\alpha)/2 \rangle L_z, \quad (28)$$

where α represents “in” or “out”; P_{xx}^α , P_{yy}^α , and P_{zz}^α are the diagonal components of the pressure tensors calculated in the local membrane regions. The outer surface tension γ^{out}

can also be calculated from the pressure tensors for the whole area.

To estimate γ^{in} and γ^{out} , we extract the inner and outer regions as follows. First, domains of type A particles are calculated. The particles are considered to belong to the same cluster (domain) when their distance is less than $r_{\text{cut}} = 2.1\sigma$. Then the radius \bar{R} of the largest domain is calculated. Type A particles contacting type B particles (closer than r_{cut}) are considered domain boundary particles. The number of boundary particles is N_{bd} . In the largest domain, the distance of the domain particles from the center \mathbf{r}_G of the domain is averaged by $R_A = (1/N_{\text{bd}}) \sum |\mathbf{r} - \mathbf{r}_G|$. For the mean radius of the domain boundary, the half boundary width $\sqrt{a_0}/2 = 0.6\sigma$ is added so that $\bar{R} = R_A + 0.6\sigma$. Then, the maximum fluctuation amplitude ΔR around \bar{R} is calculated. The surface tension γ^{in} is estimated within the area inside the circular region with radius $\bar{R} - \Delta R - 0.5\sigma$, while γ^{out} is estimated within the area outside the circular region with radius $\bar{R} + \Delta R + 0.5\sigma$. Note that a few type B particles can enter the type A domain at small $\Gamma_{AB}\sigma/k_B T \sim 1$ so the type A particles neighboring these isolated particles are not taken into account for estimation of \bar{R} and ΔR .

The line tension estimated from the 2D Laplace pressure is shown by dashed lines in Fig. 10. For the pure membrane, the obtained values agree with those from the membrane strip very well. However, they are slightly larger for the polymer-grafted membranes. This deviation is likely caused by the relative larger boundary region of the circular domain than the striped domain. It is a similar dependence obtained for the membrane edges (see Eq. 25).

B. Domain separation and microdomain formation

To clarify the grafted polymer effects, we compare the shape changes of the type A membrane domains with increasing ϕ and with decreasing ε_{AB} . In both cases, the interfacial line tension Γ_{AB} decreases and the low line tension leads to the breakup of domains. However, the resultant states are quite different as shown in Fig. 11. As the repulsive interaction between the type A and B particles is reduced with decreasing ε_{AB} , the obtained phase behavior is similar to that of typical binary fluids. At $\Gamma_{AB}\sigma \simeq k_B T$ ($\varepsilon_{AB} = 2$), the domain boundary undergoes large fluctuation and a few (type A or B) particles leave their domain to dissolve in the other domain. As ε_{AB} decreases further, the domain breaks up into small domains, and finally the two types of particles are completely mixed.

On the other hand, the grafted polymers induce formation of small stable domains (called

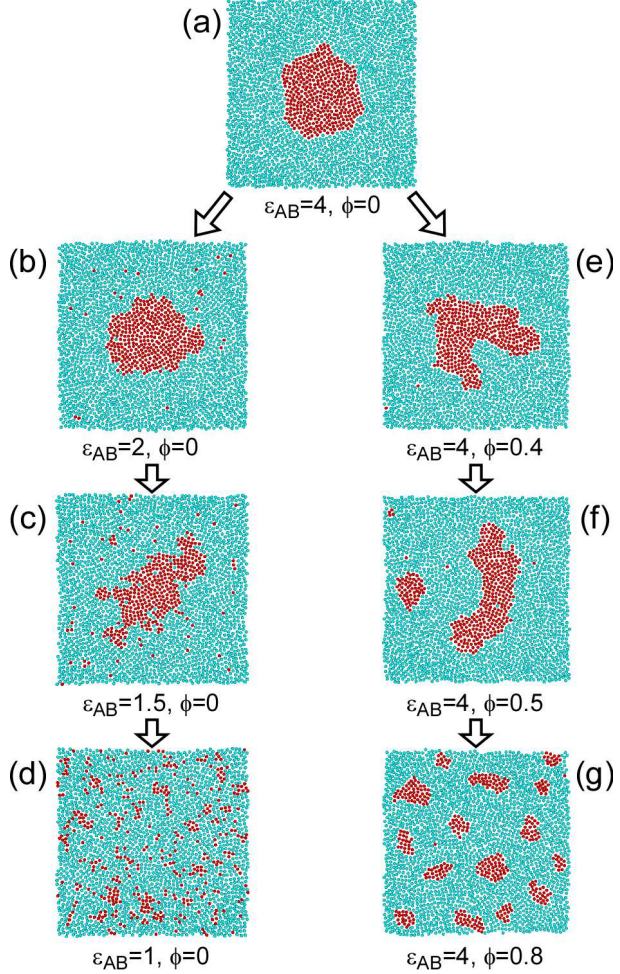


FIG. 11: Sequential snapshots of two-component membranes as (left from (a) to (d)) ε_{AB} decreases at $\phi = 0$ or (right from (a) to (g)) as the polymer density ϕ increases at $\varepsilon_{AB} = 4$. Red and blue particles represent the A and B type membrane particles, respectively. To show microdomain separation and shape transformation clearly, polymer particles are not displayed.

microdomains) instead of a mixing state, although it can reduce the line tension to $\Gamma_{AB}\sigma \lesssim k_B T$ (see Fig. 11(g)). At $\phi \leq 0.45$, the type A domain remains as one domain but exhibits an elongated shape at $\phi = 0.45$. At $\phi \geq 0.5$, it starts separating into microdomains. In contrast to the reduction in ε_{AB} , the boundary of the elongated domain is rather smooth (compare snapshots in Figs. 11(c) and (f)). Thus, the polymer effects seem suppressed for shorter lengths than the polymer size $\sim R_{\text{end}} = 4\sigma$. A smaller boundary undulation than the polymer size does not yield additional space for the polymer brush. A similar suppression in the short length scale was reported on the bending rigidity induced by the

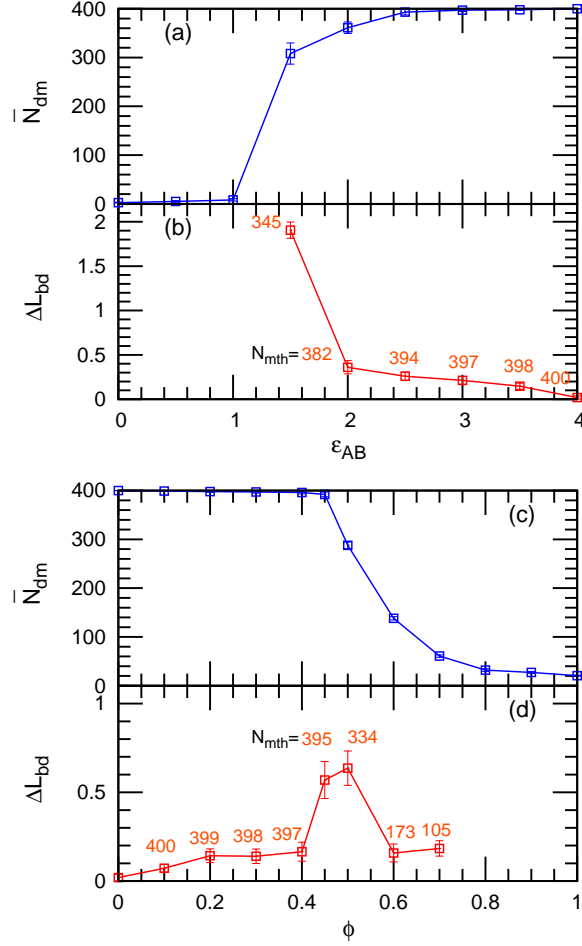


FIG. 12: Domain shape changes and domain separation as (a,b) ϵ_{AB} decreases at $\phi = 0$ and (c,d) ϕ increases at $\epsilon_{AB} = 4$. (a,c) The average cluster size \bar{N}_{dm} of the mother (largest) domains and (b,d) the reduced excess domain length ΔL_{bd} of the mother domains. The mean number N_{mth} of the membrane particles in the mother domains at each stage is shown in light red color.

polymer grafting [26]. When the domain size is comparable to the polymer length, most of the particles already stay at the domain boundary, so that an additional increase in the boundary length likely yields much less gain in the polymer conformational entropy. As explained in Sec. V A, the line tension of the circular domain is larger than the straight boundary. For the smaller domains, this difference would be enhanced, although the domains are too small for direct estimation of Γ_{AB} by Laplace's law.

To investigate the changes of domains in greater detail, we calculate the mean cluster

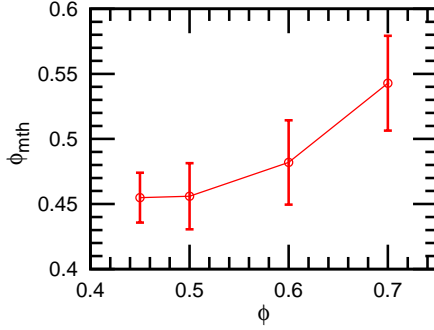


FIG. 13: Mean polymer density ϕ dependence of the number fraction ϕ_{mth} of polymer chain anchors on the mother (largest) domain.

size \bar{N}_{dm} and a reduced excess domain length ΔL_{bd} . The cluster size \bar{N}_{dm} is defined as

$$\bar{N}_{\text{dm}} = \frac{\sum_{i_c=1}^{N_{\text{A}}} n_i i_c^2}{\sum_{i_c=1}^{N_{\text{A}}} n_i i_c}, \quad (29)$$

where n_i is the number of clusters with size i_c . The reduced excess domain length for the mother (largest) domains ΔL_{bd} is defined as

$$\Delta L_{\text{bd}} = \frac{L_{\text{bd}}}{2\sqrt{\pi A_{\text{dm}}}} - 1, \quad (30)$$

where $L_{\text{bd}} = N_{\text{bd}}\sqrt{a_0}$ is the boundary length of the mother domains and $A_{\text{dm}} = N_{\text{A}}a_0$ is the domain area. The length L_{bd} is normalized by the length of a circular domain $2\sqrt{\pi A_{\text{dm}}}$ so that $\Delta L_{\text{bd}} = 0$ for the circular domain.

Figure 12 shows the development of \bar{N}_{dm} and ΔL_{bd} . In the ε_{AB} reduction, the transition to the mixing state occurs sharply between $\varepsilon_{\text{AB}} = 1.5$ and 1. However, for polymer grafting, a gradual decrease in \bar{N}_{dm} represents the formation of microdomains (see Fig. 12(c)). Around the transition points, ΔL_{bd} is increased less by polymer grafting than by lowering ε_{AB} , while both domains are similarly elongated (see Fig. 11). This difference is caused by the weaker undulation of polymer-grafted domain boundaries.

We calculated the fraction of polymer chain anchors on the mother domain ϕ_{mth} after the microdomain separation (see Fig. 13). Interestingly, it is lower than the initial density ϕ . Thus, detached small domains have higher polymer densities than their mother domain. This is caused thermodynamically by the entropy gain of polymers anchored on small domains and also kinetically by a higher density at the domain boundary.

VI. SUMMARY AND DISCUSSIONS

We have systematically studied the entropic effects of grafted polymers on various types of mechanical and interfacial properties of biomembranes using particle-based membrane simulations. First, we reconfirm the previous theoretical predictions for spontaneous curvature and bending rigidity by simulating cylindrical membranes. They increase with the anchored polymer density ϕ linearly in the mushroom region, but sharply increase in the brush region.

Second, we investigated the polymer grafting effects on the line tension of membrane edges for ideal and excluded-volume chains. It is revealed that polymer grafting significantly reduces the line tension. For ideal polymer chains, it is also investigated by a mean field theory. It is clarified that the entropy gain of polymer conformation at the membrane edge reduces the line tension. Experimentally, it is known that polymer grafting induces the formation of large vesicles [38] and spherical or discoidal micelles [40]. Since the ratio between the line tension and the bending rigidity determines the vesicle radius R_{ves} formed by the membrane disks as $R_{\text{ves}} \sim (2\kappa + \bar{\kappa})/\Gamma_{\text{ed}}$, the reduction in the line tension increases the vesicle radius. Our results are consistent with these experimental observations.

Finally, we investigated the polymer grafting effects on two-component membranes for excluded-volume chains. The line tension of the domain boundary is reduced by grafting polymers. It is found that densely grafted polymers can stabilize microdomains, whereas large domains are unstable. Although we did not investigate polymer length dependence here, it is expected that the domain size can be controlled by the polymer length. In living cells, lipid rafts contain a large amount of glycosphingolipids [4–7]. Our simulation results suggest that the entropic effects of glycosphingolipids may play a significant role in stabilizing microdomains $\lesssim 100$ nm. At a moderate polymer density, elongated shapes of membrane domains are obtained. In lipid membranes with PEG-conjugated cholesterol, the domain shapes depend on the grafted polymer density ϕ_{PEG} : at a high ϕ_{PEG} , small domains are scattered, while at a slightly lower ϕ_{PEG} , small elongated domains are connected with each other to form a network [19]. The elongated domains in our simulations may form a network, if much larger domains are simulated. Further study is needed to clarify the polymer-grafting effects on large-scale domain patterns.

Our present study highlights entropic effects of grafted polymers on the microdomain

formation via the reduction in domain boundary tension on quasi-2D biomembranes. It is well known that high line tension can induce budding of membranes. Nonzero spontaneous curvature induced by proteins and grafted polymers can lead to various liposome shapes, such as tube formation and pearlizing [51–56]. Shape transformation of vesicles induced by polymer-grafted domains is an interesting topic for further studies.

Acknowledgments

We would like to thank G. Gompper, P. A. Pincus, T. Auth, T. Taniguchi, V. N. Manoharan, and S. Komura for informative discussions. This study is partially supported by KAKENHI (25400425) from the Ministry of Education, Culture, Sports, Science, and Technology (MEXT) of Japan. HW is supported by a MEXT scholarship.

- [1] S. J. Singer and G. L. Nicolson, *Science*, 1972, **175**, 720–731.
- [2] K. Simons and E. Ikonen, *Nature*, 1997, **387**, 569.
- [3] E. Ikonen, *Curr. Opin. Cell Biol.*, 2001, **13**, 470–477.
- [4] G. Vereb, J. Szöllősi, J. Matko, P. Nagy, T. Farkas, L. Vigh, L. Matyus, T. A. Waldmann and S. Damjanovich, *Proc. Natl. Acad. Sci. USA*, 2003, **100**, 8053–8058.
- [5] S. Thomas, R. S. Kumar and T.-D. Brumeau, *Arch. Immunol. Ther. Exp.*, 2004, **52**, 215.
- [6] Z. Korade and A. K. Kenworthy, *Neuropharmacology*, 2008, **55**, 1265–1273.
- [7] L. J. Pike, *J. Lipid Res.*, 2009, **50**, S323–S328.
- [8] A. R. Honerkamp-Smith, S. L. Veatch and S. L. Keller, *Biochim. Biophys. Acta*, 2009, **1788**, 53–63.
- [9] L. Bagatolli and P. B. S. Kumar, *Soft Matter*, 2009, **5**, 3234–3248.
- [10] S. L. Veatch and S. L. Keller, *Phys. Rev. Lett.*, 2002, **89**, 268101.
- [11] T. Baumgart, S. T. Hess and W. W. Webb, *Nature*, 2003, **425**, 821–824.
- [12] A. T. Hammond, F. A. Heberle, T. Baumgart, D. Holowka, B. Baird and G. W. Feigenson, *Proc. Natl. Acad. Sci. USA*, 2005, **102**, 6320–6325.
- [13] P. I. Kuzmin, S. A. Akimov, Y. A. Chizmadzhev, J. Zimmerberg and F. S. Cohen, *Biophys. J.*, 2005, **88**, 1120–1133.

- [14] M. Yanagisawa, M. Imai and T. Taniguchi, *Phys. Rev. Lett.*, 2008, **100**, 148102.
- [15] G. G. Putzel and M. Schick, *Biophys. J.*, 2009, **96**, 4935–4940.
- [16] H. M. McConnell and V. T. Moy, *J. Phys. Chem.*, 1988, **92**, 4520–4525.
- [17] H. Wu and Z. C. Tu, *J. Chem. Phys.*, 2009, **130**, 045103.
- [18] M. Iwamoto, F. Liu and Z.-C. Ou-Yang, *EPL*, 2010, **91**, 16004.
- [19] M. Yanagisawa, N. Shimokawa, M. Ichikawa and K. Yoshikawa, *Soft Matter*, 2012, **8**, 488–495.
- [20] D. Marsh, R. Bartucci and L. Sportelli, *Biochim. Biophys. Acta*, 2003, **1615**, 33–59.
- [21] S. T. Milner and T. A. Witten, *J. Phys.*, 1988, **49**, 1951–1962.
- [22] R. Lipowsky, *Europhys. Lett.*, 1995, **30**, 197.
- [23] C. Hiergeist and R. Lipowsky, *J. Phys. II France*, 1996, **6**, 1465–1481.
- [24] H.-G. Döbereiner, O. Selchow and R. Lipowsky, *Euro. Biophys. J.*, 1999, **28**, 174–178.
- [25] T. Auth and G. Gompper, *Phys. Rev. E*, 2003, **68**, 051801.
- [26] T. Auth and G. Gompper, *Phys. Rev. E*, 2005, **72**, 031904.
- [27] M. Werner and J.-U. Sommer, *Eur. Phys. J. E*, 2010, **31**, 383–392.
- [28] E. Evans and W. Rawicz, *Phys. Rev. Lett.*, 1997, **79**, 2379–2382.
- [29] D. D. Lasic, *Angew. Chem. Int. Ed. Engl.*, 1994, **33**, 1685–1698.
- [30] A. S. Hoffman, *J. Control. Release*, 2008, **132**, 153–163.
- [31] E. W. Kaler, A. K. Murthy, B. E. Rodriguez and J. A. N. Zasadzinski, *Science*, 1989, **245**, 1371–1374.
- [32] T. M. Weiss, T. Narayanan, C. Wolf, M. Gradzielski, P. Panine, S. Finet and W. I. Helsby, *Phys. Rev. Lett.*, 2005, **94**, 038303.
- [33] J. Leng, S. U. Egelhaaf and M. E. Cates, *Europhys. Lett.*, 2002, **59**, 311–317.
- [34] D. Madenci, A. Salonen, P. Schurtenberger, J. S. Pedersen and S. U. Egelhaaf, *Phys. Chem. Chem. Phys.*, 2011, **13**, 3171–3178.
- [35] K. Bryskhe, S. Bulut and U. Olsson, *J. Phys. Chem. B*, 2005, **109**, 9265–9274.
- [36] H. Noguchi and G. Gompper, *J. Chem. Phys.*, 2006, **125**, 164908.
- [37] H. Noguchi, *J. Chem. Phys.*, 2013, **138**, 024907.
- [38] K. Bressel, M. Muthig, S. Prevost, J. Gummel, T. Narayanan and M. Gradzielski, *ACS Nano*, 2012, **6**, 5858–5865.
- [39] A. Schalchli-Plaszczynski and L. Auvray, *Eur. Phys. J. E*, 2002, **7**, 339–344.
- [40] M. Johnsson and K. Edwards, *Biophys. J.*, 2003, **85**, 3839–3847.

- [41] H. Noguchi, *J. Phys. Soc. Jpn.*, 2009, **78**, 041007.
- [42] H. Noguchi and G. Gompper, *Phys. Rev. E*, 2006, **73**, 021903.
- [43] H. Wu and H. Noguchi, *AIP Conf. Proc.*, 2013, **1518**, 649–653.
- [44] H. Noguchi, *Soft Matter*, 2012, **8**, 8926–8935.
- [45] M. P. Allen and D. J. Tildesley, *Computer Simulation of Liquids*, Clarendon Press, Oxford, 1987.
- [46] H. Shiba and H. Noguchi, *Phys. Rev. E*, 2011, **84**, 031926.
- [47] H. Noguchi, *Phys. Rev. E*, 2011, **83**, 061919.
- [48] V. A. Harmandaris and M. Deserno, *J. Chem. Phys.*, 2006, **125**, 204905.
- [49] T. V. Tolpekin, W. K. den Otter and W. J. Briels, *J. Chem. Phys.*, 2004, **121**, 8014.
- [50] B. J. Reynwar and M. Deserno, *Biointerphases*, 2008, **3**, FA117–FA124.
- [51] T. Baumgart, B. R. Capraro, C. Zhu and S. L. Das, *Annu. Rev. Phys. Chem.*, 2010, **62**, 483–507.
- [52] R. Phillips, T. Ursell, P. Wiggins and P. Sens, *Nature*, 2009, **459**, 379–385.
- [53] A. V. Shnyrova, V. A. Frolov and J. Zimmerberg, *Curr. Biology*, 2009, **19**, R772–R780.
- [54] I. Tsafir, D. Sagi, T. Arzi, M.-A. Guedea-Boudeville, V. Frette, D. Kandel and J. Stavans, *Phys. Rev. Lett.*, 2001, **86**, 1138–1141.
- [55] K. Akiyoshi, A. Itaya, S. M. Nomura, N. Ono and K. Yoshikawa, *FEBS Lett.*, 2003, **534**, 33–38.
- [56] K. Guo, J. Wang, F. Qiu, H. Zhang and Y. Yang, *Soft Matter*, 2009, **5**, 1646–1655.